Contactless Spin Switch Sensing by Chemo-Electric Gating of Graphene

Geest, E.P.; Shakouri, K.; Fu, W.; Vincent, R.; Tudor, V.; Bonnet, S.; Schneider, G.F.

Contactless Spin Switch Sensing by Chemo-Electric Gating of Graphene

Erik P. van Geest, Khosrow Shakouri, Wangyang Fu, Vincent Robert, Viorica Tudor, Sylvestre Bonnet,* and Grégory F. Schneider*

Direct electrical probing of molecular materials is often impaired by their insulating nature. Here, graphene is interfaced with single crystals of a molecular spin crossover complex, [Fe(bapbpy)(NCS)$_2$], to electrically detect phase transitions in the molecular crystal through the variation of graphene resistance. Contactless sensing is achieved by separating the crystal from graphene with an insulating polymer spacer. Next to mechanical effects, which influence the conductivity of the graphene sheet but can be minimized by using a thicker spacer, a Dirac point shift in graphene is observed experimentally upon spin crossover. As confirmed by computational modeling, this Dirac point shift is due to the phase-dependent electrostatic potential generated by the crystal inside the graphene sheet. This effect, named as chemo-electric gating, suggests that molecular materials may serve as substrates for designing graphene-based electronic devices. Chemo-electric gating, thus, opens up new possibilities to electrically probe chemical and physical processes in molecular materials in a contactless fashion, from a large distance, which can enhance their use in technological applications, for example, as sensors.

Molecular materials, that is, materials made of molecules, sometimes change their bulk properties as an effect of molecular transformations induced by external stimuli. Such materials have applications ranging from data storage, optoelectronics, photonics, nanotechnology, and quantum information processing.[1] More specifically, transition metal complexes allow the design of a great diversity of molecular

materials, particularly because the combination of metal ions and structurally diverse ligands creates a broad spectrum of chemical properties, for example, phosphorescence or magnetism. Bulk transformations in molecular materials include single-crystal-to-single-crystal transformations,[2] linkage isomerization,[3] and spin crossover (SCO) for example.[4] The sensitivity of these bulk transformations to the environment of the material makes them highly promising for sensing. However, a major drawback for the technological implementation of molecular materials for sensing is their insulating nature, which usually impairs their direct electrical readout by simple electrical measurements. Although conductive molecular materials do exist,[5] most stimulus-responsive molecular materials, for instance iron(II) compounds with SCO properties, have a negligible electrical conductivity.[6]

Remarkably, the metal-based molecules in SCO materials have the unique ability to switch between different spin states under the influence of temperature variations, light, or mechanical deformations.[7] SCO materials have been proposed as active parts of memory devices and displays,[8] mechanical actuators,[9] and sensors for temperature, pressure,[10] or the presence of small molecules.[11,12] Integration of SCO materials into electronic devices sparked the design of SCO nanoparticles and SCO thin films, specifically for the development of sensing devices and actuators.[13] Meanwhile, nanoparticles of SCO materials and single SCO molecules were also probed electrically by scanning tunneling microscopy[14] or using molecular break junctions electrodes,[15] which require complex instrumental platforms that cannot be customized into simple electronic devices. Instead, hybrid SCO materials have been proposed in the form of adsorbed particles or molecules on graphene,[16] where the conductivity of the graphene channel was related to spin-switching events in the nanoparticles.[17] However, the direct electrical readout of SCO phase changes in bulk SCO materials has been proven difficult due to their dielectric (insulating) nature.

To address this challenge, we envisioned that graphene field-effect transistors (GFETs), which are sensitive to electrostatic potential variations and have been widely used as sensing platforms,[18,19] can detect phase changes of switching molecular materials by using these materials as a substrate for

E. P. van Geest, Dr. K. Shakouri, Dr. W. Fu, V. Tudor, Dr. S. Bonnet,
Dr. G. F. Schneider
Leiden Institute of Chemistry
Leiden University
Einsteinweg 55, 2333CC Leiden, The Netherlands
E-mail: bonnet@chem.leidenuniv.nl; g.f.schneider@chem.leidenuniv.nl
Prof. V. Robert
Laboratoire de Chimie Quantique
Université de Strasbourg
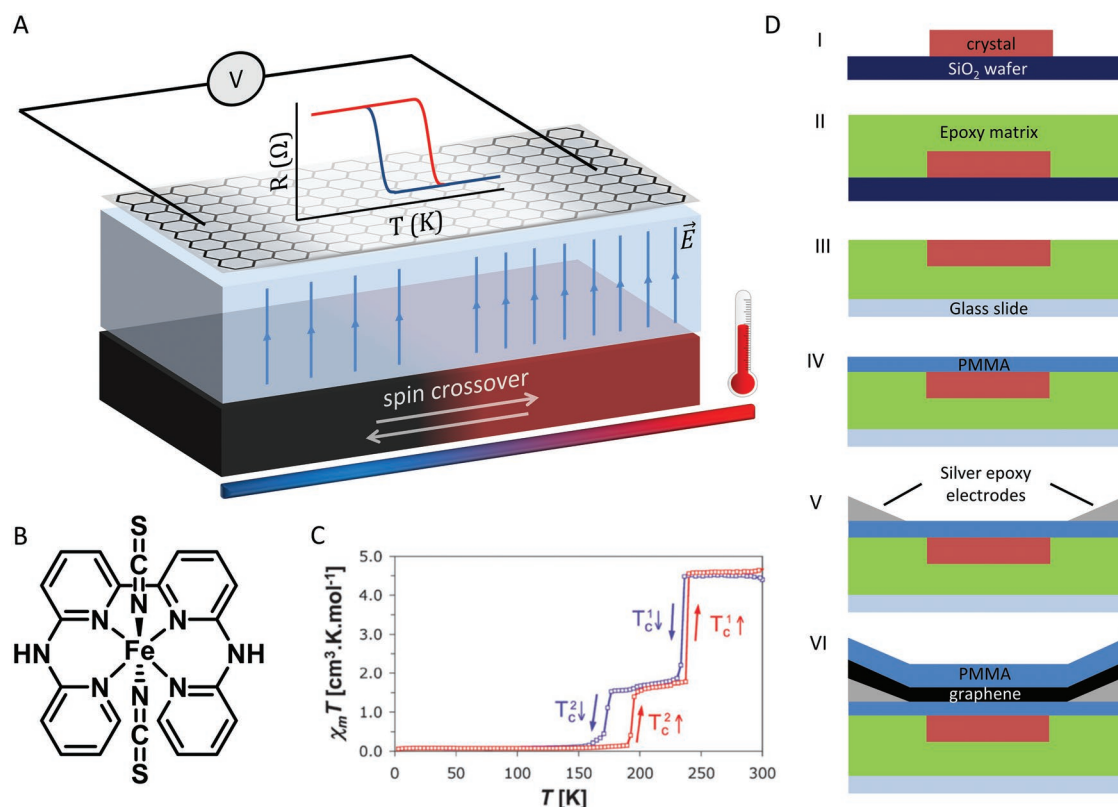CNRS
UMR 7177, 67081 Strasbourg, France

Figure 1. Device fabrication. A) Schematic representation of a graphene field-effect transistor constructed on a spin crossover (SCO) microcrystal, separated by a dielectric polymeric spacer (poly(methyl methacrylate), PMMA). Spin transitions are monitored remotely by changes in the electronic properties of graphene. B) Molecular structure of compound **1**, [Fe(bapbpy)(NCS)$_2$]. C) Magnetic susceptibility ($\chi_m T$) versus temperature for single crystals of compound **1**. C) Reproduced with permission.[21] Copyright 2008, The Royal Society of Chemistry. D) Side view step-by-step schematic representation of the fabrication of graphene transistors on SCO crystals. I: Single crystal of compound **1** grown on Si/SiO$_2$ wafer; II: crystal on wafer cast in epoxy resin; III: epoxy, holding crystal pulled from wafer and placed upside down on a microscope cover glass; IV: PMMA film transferred onto the epoxy and the crystal; V: solid silver epoxy electrodes placed close to crystal edges; VI: transfer of a PMMA–graphene film and removal of excess graphene to finish the device.

the GFET (see **Figure 1**A). More specifically, single crystals of the coordination compound [Fe(bapbpy)(NCS)$_2$] (compound **1**, where bapbpy = N,N′-di(pyrid-2-yl)-2,2′-bipyridine-6,6′-diamine; see Figure 1B) were chosen to serve as a substrate for graphene. These crystals reversibly undergo abrupt, thermally induced SCO phase transitions (see Figure 1C) without suffering from mechanical damage,[20,21] in contrary to other SCO materials.[22] Direct electrical probing of the molecular state of the SCO crystals was achieved in GFETs fabricated over SCO crystals of **1** using a concept called "chemo-electric gating" (CEG). CEG occurs through the generation of an electrostatic potential inside the graphene sheet, generated by the single crystal. Although mechanical stress induced by the SCO phenomenon also contributes to variations of the conductivity of the graphene sheet, separating the crystal and the graphene sheet by a thick (0.5 μm) polymer spacer minimized mechanical stress so that variations of the electric dipole fluctuation of each spin-switching molecule inside the crystal lead to variations of the Dirac point of the graphene sheet, which is sensed through simple electrical readout. Importantly, CEG allows contactless sensing, as the SCO substrate and GFET are electrically and physically separated by a dielectric spacer that is only permeable to electrostatic effects induced by the SCO material. The

polymer spacer appears, hence, as a critical component of such devices, as it separates graphene from the environment of the SCO material and protects it from the mechanical effects of SCO, without hampering the direct detection of the molecular transformations occurring within the SCO crystal.

GFETs on SCO single crystals were fabricated from single crystals of compound **1**, typically few hundreds of micrometers in length and tens of micrometers in width, grown from a DMF/methanol solution directly on silicon wafers (Figure 1D,I).[21] The crystals were cast in a flexible epoxy resin. The resin sheet embedding the crystals was removed from the wafer (II) and a slab with one single crystal only was cut from the resin sheet, and then placed on a thin glass slide with the crystal facing upwards (III). A poly(methyl methacrylate) (PMMA) spacer was then transferred on top of the crystal (IV). Source and drain electrodes were constructed close to the crystal using a silver-based epoxy and connected with copper wires (V). Finally, a sheet of PMMA–graphene was transferred on top of the spacer—thus sandwiching graphene between the PMMA layers—and the excess of PMMA–graphene was removed mechanically to complete the device (VI, for a photo and top view schematic representation, see Figure S1 and S2, Supporting Information). The deposition of a film-like material

on the otherwise flat surface of the crystals was confirmed by atomic force microscopy and Raman spectroscopy (see Figure S3, Supporting Information). Transistors typically had electrical resistance values up to 20 kΩ between the source and the drain electrodes of the device.

Next, GFETs on SCO crystals were subjected to iterative cooling–heating cycles to trigger the SCO events in the crystal. Notably, the SCO properties of the crystals used in this study appeared not to have been influenced by embedding them into the epoxy matrix; the transition temperatures and rates of the transitions were very similar to those of free crystals. Each SCO occurring between phase I, the phase observed at high temperature, where all molecules are high spin (HS), and phase II, the phase at intermediate temperatures where two-third of the molecules are low spin (LS) and one-third remains in the HS state,[21] could be observed optically by a swift color change from red (phase I) to black (phase II, see Video S1, Supporting Information). Most importantly, each color change was accompanied by an abrupt change in the resistance R of graphene (see **Figure 2**A,B, device with 0.5 μm spacer and Video S2, Supporting Information). Similarly, resistance variations were also observed for the transition between phase II to phase III, where all molecules in the crystal are LS; however, this second transition was not studied extensively because of the difficulty to optically observe this second transition, together with the general technical difficulties of operating the SCO-graphene devices at very low temperatures (see Figure S4 and S5,

Supporting Information). All results below are hence described for the high-temperature SCO only, that is, the SCO between phase I and phase II.

For devices with the thickest spacer (0.5 μm), the direction of SCO was captured in the sign of dR/dt; phase transitions gave peaks that are positive for phase I to II and negative for the reverse transition (see Figure 2C, black). As controls, graphene transistors were fabricated on an epoxy matrix without the presence of SCO crystals. The electrical resistance of these transistors did not show systematic abrupt variations and no distinct peaks were observed in dR/dt, even after four consecutive temperature sweep-cycles (Figure 2C, green). As shown in Figure 2A, R and the relative fraction of molecules in crystals of **1** that are the HS state (x_{HS}), as measured by magnetic susceptibility measurements, were directly related during the temperature cycling: R and x_{HS} drastically varied at identical temperatures, that is, the temperatures at which the phase transitions in fact occur. Thus, the graphene transistors successfully sensed the SCO events, regardless of the thick PMMA layer (0.5 μm) separating the graphene sheet from the SCO single crystal.

During these experiments, the SCO properties of the crystal were retained as the device passed through several transition cycles. Notably, both transition temperatures, $T_c\uparrow$ and $T_c\downarrow$, remained unaffected and the hysteresis loop continued to exist without significant variation of its width. The first transition usually occurred at a slightly lower temperature (see Figure 2A), which we interpret as a consequence of defect formation during
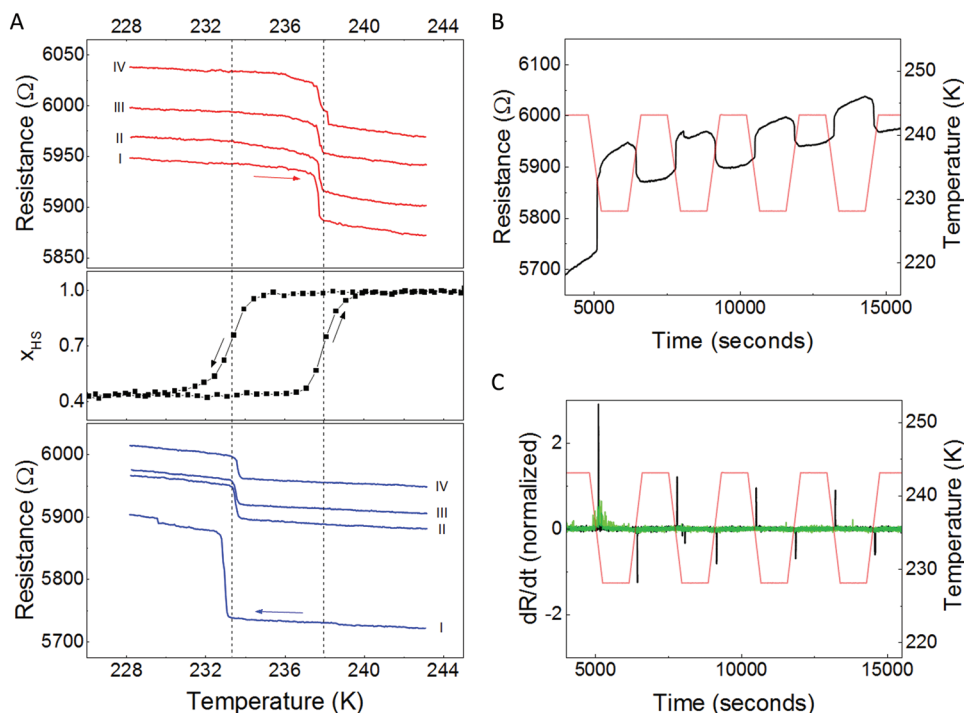

Figure 2. Electrical detection of spin phase transitions by chemo-electric gating. A) Electrical resistance (blue, red) and fraction x_{HS} of high spin molecules in the SCO material versus temperature (connected squares) obtained from magnetic susceptibility measurements on SCO crystals grown on a silicon wafer; the electrical resistance during four heating/cooling cycles (indicated I–IV) in the SCO temperature region is indicated as red (heating at 2 K min^{-1}; top) and blue (cooling at 2 K min^{-1}; bottom), respectively. Dotted lines indicate phase transition temperatures from magnetic susceptibility measurements. B) Electrical resistance (black) and temperature (red) over time for a typical graphene transistor constructed on a single crystal of compound **1** (spacer thickness = 0.5 μm). C) dR/dt, normalized for R just before the first transition, and temperature versus time; graphene on a single crystal of **1** with a 0.5μm spacer in black, reference graphene on epoxy without crystal in green.

**ADVANCED
SCIENCE NEWS**
www.advancedsciencenews.com

**ADVANCED
MATERIALS**
www.advmat.de

the first SCO event. Cracks appearing in the crystal during the first transition may propagate during the following transitions (see Figure S6, Supporting Information). Indeed, defects are known to serve as nucleation points for the phase transition in crystals of **1**;[23] an increase in defects could therefore trigger the phase transition earlier (i.e., at slightly higher temperatures in the cooling mode) as more nucleation sites are available.

As such mechanical effects may have consequences on the integrity and conductivity of the graphene sheet lying on top of it, we studied the influence of the thickness of the polymeric PMMA spacer, that is, the distance between the graphene sheet and the crystal, on $\Delta R/R_0$ upon series of SCO transitions. The thickness of the spacer was adjusted by using different spin coating rates (step IV in Figure 1D). The electrical resistance of the GFET with the different spacers was monitored while the temperature was cycled from below and above the phase transition temperatures. Remarkably, regardless of the spacer thickness (0 µm = no spacer, 0.1, 0.3, or 0.5 µm), the graphene devices responded to the SCO events. The electrical response to a SCO event, however, drastically decreased for increasing PMMA spacer thicknesses. As indicated above, with the thickest spacer (0.5 µm), the sign of the resistance variation $\Delta R/R_0$—where ΔR is the resistance difference before and after the phase transition and R_0 is the resistance right before the transition—was in agreement with the SCO direction (i.e., from phase I to phase II and vice versa): $\Delta R/R_0$ was positive when the crystal went from phase I to phase II and negative for reverse transitions. On the other hand, for devices with a spacer thickness of 0.1 µm or lower, the resistance always increased upon SCO, that is, independently of the direction of the spin transition, while for a spacer of 0.3 µm, the sign of $\Delta R/R_0$ was always positive from phase I to II transitions but no clear trend was visible for the reverse II to I transitions (see **Figure 3**A,B; for resistance vs time and dR/dt vs time for devices with different spacers, see Figure 2B,C; Figure S7–S9, Supporting Information). Moreover, for devices with a spacer of 0.3 µm or lower, $\Delta R/R_0$ decreased with an increasing number of SCO cycles, while for devices with a spacer of 0.5 µm, $\Delta R/R_0$ did not vary strongly between up to four SCO cycles. Thus, a decrease in $\Delta R/R_0$ for the next phase transitions seemed to be

mitigated by the overall increased distance between graphene and the SCO crystal, signifying a "buffering" effect imposed by the spacer. Clearly, the polymer spacer plays a critical role in the sensing mechanism, which may rely on a combination of mechanical and electrical effects (see below).

Mechanical effects induced by a phase-transition in SCO materials are caused by the different volume of the coordination sphere of the metal complex in the HS and LS states, which is known to induce macroscale damages to SCO crystals.[24] Although single crystals of compound **1** typically do not suffer appreciably from such mechanical damage as they undergo repeated SCO cycling (see Figure S6, Supporting Information), the crystal lattice contracts (phase I to II) or expands (phase II to I) during SCO events,[21] which could mechanically stress the graphene sheet. To study strain effects arising from the phase transitions and the "buffering" effect of the spacer, the graphene sheet in electrode-free devices with different spacer thicknesses was inspected with Raman spectroscopy during multiple SCO cycles. Uniaxial strain is known to cause a red-shift of the 2D peak in the Raman spectrum of graphene.[25] Indeed, a clear peak shift of the 2D peak occurred after the first transition, independent of the spacer thickness (phase I to II, see **Figure 4**A), while no significant shifts were observed during the following transitions (see Figure 4B). These results indicate that graphene was mechanically strained during the first phase transition. This effect appears to be a strong contributor to the exceptionally high resistance variation (in the positive direction) at the first transition. For the following transitions, any shifts in the 2D peak would be hidden by the large error bars, preventing any conclusion to be drawn about mechanical strain during these transitions; mechanical strain thus cannot be excluded from the sensing mechanism of the SCO events by such devices, but it was minimized by using thicker spacers. The standard deviation of the 2D peak position increased most strongly in the absence of spacer, indicating a decreased homogeneity of the graphene, possibly due to mechanical damage. A 0.5 µm PMMA spacer appeared to optimally reduce the mechanical stress or damage to the graphene sheet during spin transitions; the mechanistic studies described below used devices with 0.5 µm spacer thickness.
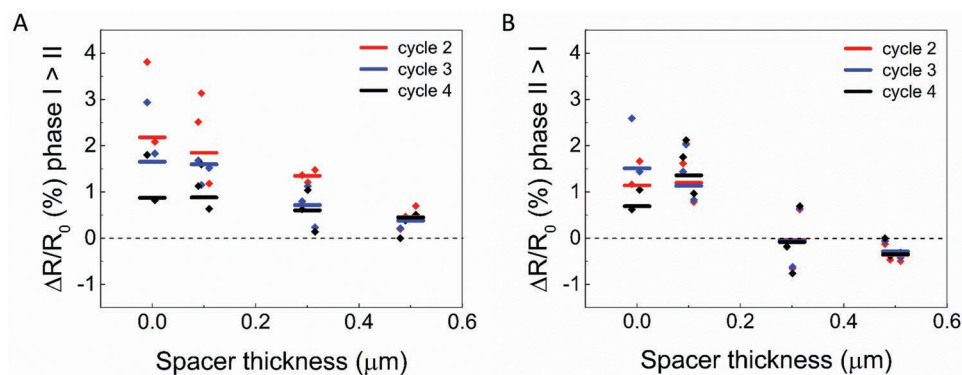

Figure 3. Remote detection of spin crossover with different spacer thicknesses. $\Delta R/R_0$ for devices with PMMA films of various thicknesses (0, 0.1, 0.3, and 0.5 µm). A) Device response to phase I to phase II transitions (cycle 2–4, respectively, blue, red, and green; horizontal bars represent average values of three devices, diamonds represent $\Delta R/R_0$ for individual devices). SCO cycle 1 is not regarded as $\Delta R/R_0$ was typically significantly higher than in following cycles, which we believe is due to initial defect formation during the first transition. B) Device response for phase II to I transitions, cycle 2 to 4 (color and symbol code the same as panel A). SCO cycle 1 is not regarded here as well.
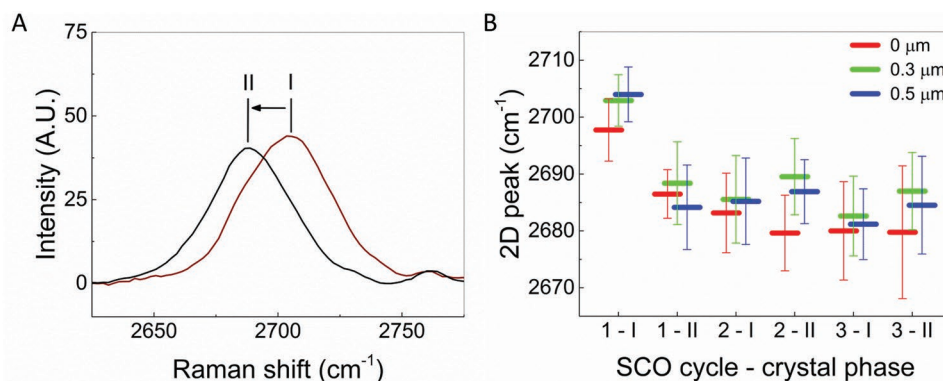
Figure 4. Raman spectroscopy study of electrode-free devices with different spacer thicknesses undergoing multiple spin crossover events. A) 2D peak for phase I at 243 K and phase II at 223 K in the first SCO cycle (respectively, red and black, averages of 16 individual locations, 0.3 µm spacer). The spin transition caused the 2D peak of graphene to shift from 2704 to 2689 cm^{-1}, an indication of mechanical strain applied to graphene. B) 2D peak after multiple transitions (spacer thickness: blue = 0 µm, red = 0.3 µm, green = 0.5 µm), each bar represents the average of 16 individual measurements at different locations on the coated crystal.

To further elucidate the SCO-sensing mechanism of the devices, a gate electrode based on an ionic liquid (IL) was constructed on top of a graphene transistor for I/V characterization (see **Figure 5**A). To do so, the transistor was constructed with a PMMA-IL mixed film on graphene instead of pure PMMA, for gating purposes. The device was then

exposed to oxygen plasma to completely remove the excess of graphene (Figure S2B, IV, Supporting Information). Source and drain electrodes were protected with a dielectric epoxy resin (VII) and a droplet of the IL diethylmethyl(2-methoxyethyl)ammonium bis(trifluoromethylsulfonyl)imide (DEME-TFSI) was placed over the crystal, which was connected with
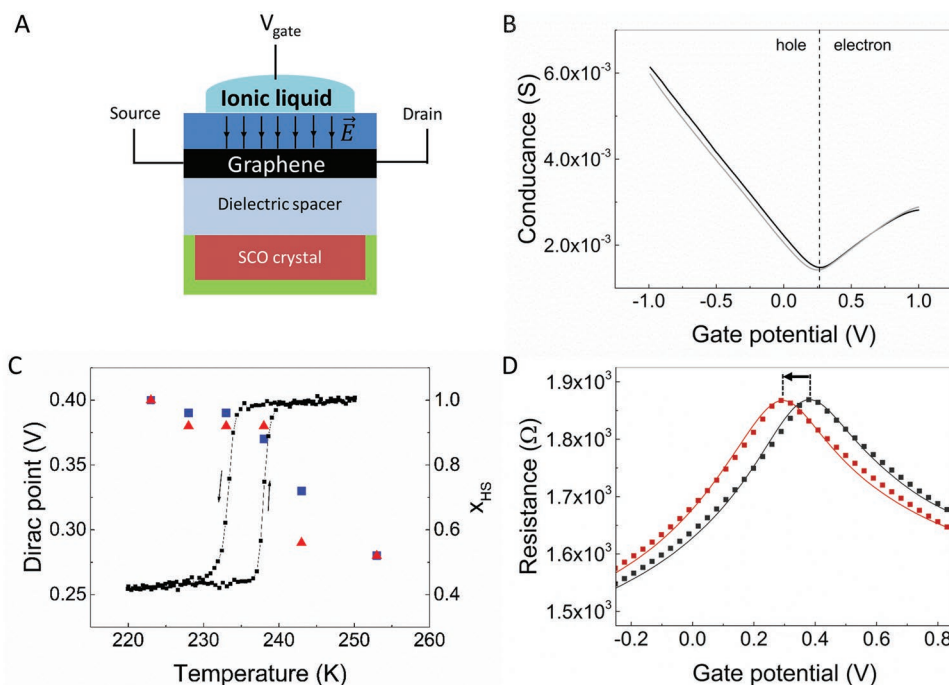

Figure 5. Dirac point shift induced by a spin phase transition in a top-gated GFET. A) Side-view schematic illustration of a top-gated GFET. The ionic liquid DEME-TFSI was used as it has a particularly low glass transition temperature (182 K), required for low-temperature gating.[27] Liquid gating was performed through a mixed PMMA/DEME-TFSI (3:1) layer on graphene, with a droplet of the ionic liquid on top of this mixed layer for electrical contact. B) Conductance versus gate potential at 293 K before and after one temperature cycle (black and gray, respectively). To obtain the conductance of the graphene sheet, the contact resistance was subtracted by assuming linear conductance decrease away from the Dirac point in the hole regime, as the conductivity of graphene in pure hole or electron regions is known to be linearly proportional to the gate potential.[18] C) Dirac point (left axis, blue squares and red triangles for the cooling and heating modes, respectively) and fraction x_{HS} of HS molecules in the SCO crystal (black squares, as determined by SQUID magnetic susceptibility measurements) versus temperature. D) Resistance versus gate potential for high spin (phase I at 243 K, red line) and intermediate phase (phase II at 238 K, black line) from experimental work (lines, red and black for phase I and II, respectively) and fitting (squares, red and black for phase I and II, respectively) based on computational work. The arrow shows the direction of the Dirac point shift during a transition from phase II to phase I.

a copper foil electrode to finalize the gate on top of the crystal (Figure S2B, VIII and Figure S1, Supporting Information). When the gate voltage was swept between –1 V and +1 V, the ambipolar behavior of graphene was observed: the conductance of the graphene sheet ($1/R$), first decreased to reach a minimum (the Dirac point) and then immediately increased again (see Figure 5B, for resistance vs gate potential, see Figure S10, Supporting Information).

This behavior arises from the zero-gap semiconducting nature of graphene, which has two distinct conductivity regimes. In the "hole conductivity" regime, the charge carriers are positively charged electron holes in the electron-deficient valence band, promoted by the negative electrostatic potential from the gate. In the "electron conductivity" regime, on the other hand, the charge carriers are free electrons in the conductance band. At the Dirac point, the valence band is full and the conductance band is empty, the carrier concentration and thus the conductance are minimal, that is, the resistance is maximal.[18,26] In general, the filling of both bands is governed by the Fermi level, which can be altered by an electrostatic potential supplied by the gate electrode; hence, the conductivity of the device responded to the changing gate voltage.

Interestingly, the ambipolar behavior was sensitive to spin phase transitions in the SCO crystal, which were thermally induced while performing the I/V characterization of the GFET. From 293 to 223 K, the ambipolar behavior was always characterized by a Dirac peak between 0.2 and 0.4 V. Moreover, the Dirac point shifted over 0.1 V in the SCO temperature range both during the cooling and heating trajectory (see Figure 5C; Figure S11, Supporting Information). This shift showed that the positive doping of the graphene sheet was higher at temperatures below the spin transition temperature, which indicates that the phase II of the crystal induced an increased doping; the SCO crystal thus performed CEG. This positive doping resulted in a variation in resistance when the gate voltage was fixed (see Figure 5D); this is also what was observed for the devices operated without a gate electrode. Therefore, the variations in resistance in these devices arose from a Dirac point shift of the GFET, as graphene was doped differently by phase I or II of the CEG-substrate, suggesting that, next to mechanical interactions, electrostatic interactions were clearly involved in the sensing of the spin transitions by graphene.

At this point, we hypothesized that the Dirac point shift, and hence part of the resistivity variations of the GFET, was a consequence of long-distance CEG of graphene by the crystal. Building on preceding electronic structure calculations,[28] we indeed realized that the charge distribution of an individual molecule of **1** is subject to significant variations during a spin transition, which will affect the electrostatic potential created by the crystal inside the graphene sheet (see Supporting Information). To support our hypothesis, we quantitatively examined the electrostatic potential induced by the SCO crystal in graphene. For simplicity, we modeled the crystal surface by a set of parallel charged sheets stacked on top of each other. Each sheet consists of a 2D array of identical atoms whose charge density is distributed uniformly along the extension direction of the surface. As the charges borne notably by the Fe and N atoms of the complex (see Table S2, Supporting Information) are different in the HS and LS states, not only the spacing between

the charged sheets, but also the charge density borne by each sheet in phase I and II, are different; thus, the electrostatic potential induced in graphene by each sheet in either phase I or II is different. For a thick crystalline slab of ≈21–129 µm, the potential difference created in graphene between phase I and II was calculated to be ≈17–100 mV (see Supporting Information), thus confirming theoretically the Dirac point shift observed experimentally when the crystal switched from one spin phase to the other (see Figure 5D). We note, however, that our model of stacked charged sheets offers a uniform electrostatic potential outside the crystal. Practically speaking, this approximation holds true as long as the length and width of the crystal surface are much larger than the distance between the graphene sheet and the crystal substrate, which was the case in our devices.

Based on this idea, our theoretical approach to model the resistivity ρ of graphene and fit experimental data accounts for the effect of electron–phonon coupling (ρ_{e-ph}),[29] and of long-range scattering by the Coulomb potential of charged impurities (ρ_c),[30–33] which according to Matthiessen's rule yields

$$\rho = \rho_{e-ph} + \rho_c \tag{1}$$

Both ρ_{e-ph} and ρ_c were calculated as functions of the top-gate voltage V_g using the semiclassical Boltzmann transport theory,[30] although the phonon-limited resistivity ρ_{e-ph} has been found to have only a minor contribution at the experimental temperatures $T = 238$ and 243 K (ρ_{e-ph} is roughly two orders of magnitude smaller than ρ_c). In contrast, the inclusion of charge impurities is essential to reproduce the experimental results especially in view of the following two aspects: first, the measured charge conductivity (σ) varies approximately linearly at high carrier densities (n), which can be traced back to long-range electrostatic interactions with charged impurities;[32,33] second, the conductivity minimum near the neutrality point is indeed an indication of a residual carrier density n^* that can be induced by inhomogeneous potential fluctuations due to charged impurities.[32] Making use of a self-consistent theory as described by Adam et al.,[32] the experimental resistance was well reproduced for the values of $n^* = 7.2 \times 10^{11}$ cm^{-2} and $n_i = 1.4 \times 10^{12}$ cm^{-2}, where n_i is the density of impurities (see Figure 5D and Supporting Information). On the basis of this theory and given the linearity of σ in n, the mobility of graphene was calculated to be $\mu = \sigma/ne \approx 4.8 \times 10^2$ cm^2 V^{-1} s^{-1}. Overall, the excellent fit between the experiment and theory observed in Figure 5D suggests that when the PMMA spacer is thick enough (0.5 µm), CEG is largely responsible for the contactless sensing of SCO by GFETs. It should be noted that the different magnetic properties of **1** in the different spin states do not contribute here to the sensing mechanism. Whether diamagnetic or paramagnetic, the SCO crystal has no net magnetic moment in absence of an externally applied magnetic field. We can thus exclude that the changing magnetic susceptibility of the crystal upon SCO has any contribution to the resistance variations of the GFETs.

In order to interpret how CEG affects the transport properties of graphene simultaneously with spin switches in the crystal, one should solely consider the electrostatic effects occurring when the crystal undergoes SCO. As shown schematically in **Figure 6**, the electric dipole moment $\vec{p}$ of each molecule
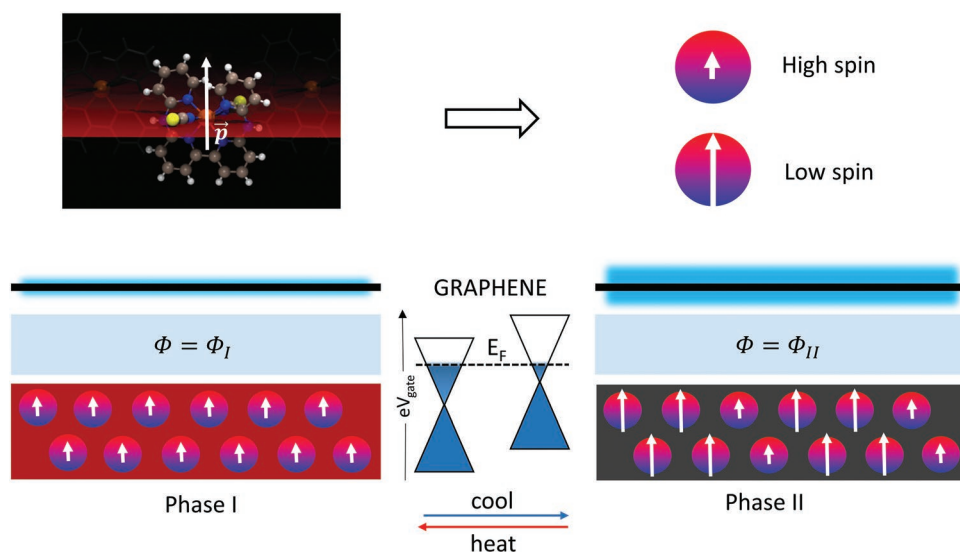
Figure 6. Schematic representation of chemo-electric gating of graphene. Due to changes in the electric dipole ($\vec{p}$, white arrows) of individual molecules in the SCO crystal, the electrostatic potential (Φ) between the SCO crystal and graphene changes, which affects the Fermi level and thus electrical properties of graphene.

of $[Fe(bapbpy)(NCS)_2]$ depends drastically on its spin state. Electronic structure calculations indicate that a spin switch shifts the molecular dipole moment by more than a factor 3: in the HS state, each molecule has a dipole moment of 1.1901 Debye, while in the LS state, its dipole moment increases to 3.8958 Debye, giving a difference of 2.7057 Debye between the different states (see Table S2, Supporting Information). Such a change is essentially the result of two electrons relocating from t_{2g} to e_g orbitals when the molecule goes from the LS to the HS state, and hence moving away from the metal toward the nitrogen ligands (see Figure 6). Since the molecules are ordered in a single crystalline material, the dipole moments of individual molecules add up, which creates an electrostatic potential outside the crystal that interacts with the graphene sheet in a spin state-dependent manner. When a SCO event occurs and a large fraction of the molecules (two-third) switch their dipole moment from HS to LS at once, the electrostatic potential induced by the crystal changes in strength, and thereby modifies the Fermi level of graphene. When the gate potential is fixed, such modifications of the Fermi level can induce large changes up to 73 Ω in the resistance of graphene (see Figure 5D).

Usually, sensing SCO in (nano)materials relies on variations of magnetic moments,[4] color variations,[12] or differences in fluorescence quenching by the HS and LS molecules.[34] In contrast, the mechanism described here relies on a combination of mechanical stress and of the electrostatic changes occurring in a SCO molecule undergoing a spin transition. This mechanism not only demonstrates that the electrostatic component of the SCO switch is strong enough to build sensors capable of detecting SCO, it also opens new routes for using combinations of graphene and molecular materials to build electronic devices capable of contactless sensing, that is, sensing without the electronic part of the sensor having to be in direct contact with the sensed environment. Contactless sensing may also provide a protecting layer (the spacer in this case) preventing the electronic parts of the sensor to be in direct contact with the environment being sensed, which may lead to more stable devices.

Based on experimental and computational investigations, we demonstrate here that phase transitions in single crystals of an electrically insulating SCO material can be probed electrically by a graphene transistor separated from the SCO crystal by a 0.5 µm-thick polymer spacer. Sensing is governed largely by CEG, that is, a variation of the Fermi level in graphene induced by the spin transition of a large number of SCO molecules, and partly by mechanical deformations of the graphene sheet (induced by cracks in the crystal undergoing SCO) that were minimalized by the polymer spacer. Because the intrinsic doping of graphene by the electrostatic potential generated by the molecular changes when the phase of the crystal changes, the Dirac point and resistance of the GFET change as well. This resistance variation, which is a direct effect of the SCO event, can be easily measured by standard electronic equipment. We also discovered that the thickness of the polymer layer (at least three orders of magnitude thicker than graphene) between the crystal and graphene must be high enough to minimize mechanical effects and obtain robust and reproducible signals arising mostly from CEG. Our design represents a new and versatile method to obtain electrical readout of SCO in large crystalline substrates, while the region where molecular switching occurs—the SCO crystal—and the detection circuit—the graphene sheet—are electrically separated. We believe the advantages of CEG of graphene offer an additional design strategy toward graphene-based sensing technologies, as it allows for obtaining straightforward electrical readout of a remote change at the molecular level that impacts the dipole moment of the molecules in a material. Of course, we have focused here on thermally induced SCO, but we believe that this platform may be used also to fit a wide range of functional molecular materials where a change in the environment of the materials translates into a variation of the dipole moment of molecules.

Supporting Information

Supporting Information is available from the Wiley Online Library or from the author.

Conflict of Interest

The authors declare no conflict of interest.

Keywords

chemo-electric gating, contactless sensing, graphene, molecular materials, spin crossover

[1] D. W. Bruce, D. O'Hare, R. I. Walton, *Molecular Materials*, Wiley, New York **2011**.

[2] A. Chaudhary, A. Mohammad, S. M. Mobin, *Cryst. Growth Des.* **2017**, *17*, 2893.

[3] a) J. J. Rack, J. R. Winkler, H. B. Gray, *J. Am. Chem. Soc.* **2001**, *123*, 2432; b) M. R. Warren, S. K. Brayshaw, A. L. Johnson, S. Schiffers, P. R. Raithby, T. L. Easun, M. W. George, J. E. Warren, S. J. Teat, *Angew. Chem., Int. Ed.* **2009**, *48*, 5711.

[4] P. Gütlich, A. B. Gaspar, Y. Garcia, *Beilstein J. Org. Chem.* **2013**, *9*, 342.

[5] a) C. Faulmann, K. Jacob, S. Dorbes, S. Lampert, I. Malfant, M.-L. Doublet, L. Valade, J. A. Real, *Inorg. Chem.* **2007**, *46*, 8548; b) K. Takahashi, H.-B. Cui, Y. Okano, H. Kobayashi, Y. Einaga, O. Sato, *Inorg. Chem.* **2006**, *45*, 5739.

[6] A. Rotaru, I. A. Gural'skiy, G. Molnár, L. Salmon, P. Demont, A. Bousseksou, *Chem. Commun.* **2012**, *48*, 4163.

[7] J. A. Real, A. B. Gaspar, M. C. Munoz, *Dalton Trans.* **2005**, 2062.

[8] O. Kahn, J. Kröber, C. Jay, *Adv. Mater.* **1992**, *4*, 718.

[9] H. J. Shepherd, I. A. Gural'skiy, C. M. Quintero, S. Tricard, L. Salmon, G. Molnár, A. Bousseksou, *Nat. Commun.* **2013**, *4*, 2607.

[10] C.-M. Jureschi, J. Linares, A. Boulmaali, R. P. Dahoo, A. Rotaru, Y. Garcia, *Sensors* **2016**, *16*, 187.

[11] a) P. D. Southon, L. Liu, E. A. Fellows, D. J. Price, G. J. Halder, K. W. Chapman, B. Moubaraki, K. S. Murray, J.-F. Létard, C. J. Kepert, *J. Am. Chem. Soc.* **2009**, *131*, 10998; b) G. J. Halder, C. J. Kepert, B. Moubaraki, K. S. Murray, J. D. Cashion, *Science* **2002**, *298*, 1762; c) S. M. Neville, G. J. Halder, K. W. Chapman, M. B. Duriska, B. Moubaraki, K. S. Murray, C. J. Kepert, *J. Am. Chem. Soc.* **2009**, *131*, 12106; d) X. Bao, H. J. Shepherd, L. Salmon, G. Molnár, M.-L. Tong, A. Bousseksou, *Angew. Chem., Int. Ed.* **2013**, *52*, 1198.

[12] M. Ohba, K. Yoneda, G. Agustí, M. C. Muñoz, A. B. Gaspar, J. A. Real, M. Yamasaki, H. Ando, Y. Nakao, S. Sakaki, S. Kitagawa, *Angew. Chem., Int. Ed.* **2009**, *48*, 4767.

[13] a) K. Senthil Kumar, M. Ruben, *Coord. Chem. Rev.* **2017**, *346*, 176; b) G. Molnár, S. Rat, L. Salmon, W. Nicolazzi, A. Bousseksou, *Adv. Mater.* **2018**, *30*, 1703862; c) C. Lefter, V. Davesne, L. Salmon, G. Molnár, P. Demont, A. Rotaru, A. Bousseksou, *Magnetochemistry* **2016**, *2*, 18; d) G. Molnar, L. Salmon, W. Nicolazzi, F. Terki, A. Bousseksou, *J. Mater. Chem. C* **2014**, *2*, 1360; e) S. Suárez-García, N. N. Adarsh, G. Molnár, A. Bousseksou, Y. Garcia, M. M. Dîrtu, J. Saiz-Poseu, R. Robles, P. Ordejón, D. Ruiz-Molina, *ACS Appl. Nano Mater.* **2018**, *1*, 2662.

[14] a) T. Jasper-Toennies, M. Gruber, S. Karan, H. Jacob, F. Tuczek, R. Berndt, *Nano Lett.* **2017**, *17*, 6613; b) T. G. Gopakumar, F. Matino, H. Naggert, A. Bannwarth, F. Tuczek, R. Berndt, *Angew. Chem., Int. Ed.* **2012**, *51*, 6262; c) T. Miyamachi, M. Gruber, V. Davesne, M. Bowen, S. Boukari, L. Joly, F. Scheurer, G. Rogez, T. K. Yamada, P. Ohresser, E. Beaurepaire, W. Wulfhekel, *Nat. Commun.* **2012**, *3*, 938; d) A. C. Aragonès, D. Aravena, J. I. Cerdá, Z. Acís-Castillo, H. Li, J. A. Real, F. Sanz, J. Hihath, E. Ruiz, I. Díez-Pérez, *Nano Lett.* **2016**, *16*, 218.

[15] a) G. D. Harzmann, R. Frisenda, H. S. J. van der Zant, M. Mayor, *Angew. Chem., Int. Ed.* **2015**, *54*, 13425; b) F. Prins, M. Monrabal-Capilla, E. A. Osorio, E. Coronado, H. S. J. van der Zant, *Adv. Mater.* **2011**, *23*, 1545.

[16] a) M. Bernien, H. Naggert, L. M. Arruda, L. Kipgen, F. Nickel, J. Miguel, C. F. Hermanns, A. Krüger, D. Krüger, E. Schierle, E. Weschke, F. Tuczek, W. Kuch, *ACS Nano* **2015**, *9*, 8960; b) D. Qiu, D.-H. Ren, L. Gu, X.-L. Sun, T.-T. Qu, Z.-G. Gu, Z. Li, *RSC Adv.* **2014**, *4*, 31323; c) K. Senthil Kumar, I. Šalitroš, Z. Boubegtiten-Fezoua, S. Moldovan, P. Hellwig, M. Ruben, *Dalton Trans.* **2018**, *47*, 35.

[17] J. Dugay, M. Aarts, M. Giménez-Marqués, T. Kozlova, H. W. Zandbergen, E. Coronado, H. S. J. van der Zant, *Nano Lett.* **2017**, *17*, 186.

[18] K. S. Novoselov, A. K. Geim, S. V. Morozov, D. Jiang, Y. Zhang, S. V. Dubonos, I. V. Grigorieva, A. A. Firsov, *Science* **2004**, *306*, 666.

[19] a) D. Hernández-Sánchez, G. Villabona-Leal, I. Saucedo-Orozco, V. Bracamonte, E. Pérez, C. Bittencourt, M. Quintana, *Phys. Chem. Chem. Phys.* **2018**, *20*, 1685; b) W. Fu, L. Jiang, E. P. van Geest, L. M. C. Lima, G. F. Schneider, *Adv. Mater.* **2017**, *29*, 1603610.

[20] S. Bonnet, G. Molnár, J. Sanchez Costa, M. A. Siegler, A. L. Spek, A. Bousseksou, W.-T. Fu, P. Gamez, J. Reedijk, *Chem. Mater.* **2009**, *21*, 1123.

[21] S. Bonnet, M. A. Siegler, J. S. Costa, G. Molnar, A. Bousseksou, A. L. Spek, P. Gamez, J. Reedijk, *Chem. Commun.* **2008**, 5619.

[22] Y. Miyazaki, T. Nakamoto, S. Ikeuchi, K. Saito, A. Inaba, M. Sorai, T. Tojo, T. Atake, G. S. Matouzenko, S. Zein, S. A. Borshch, *J. Phys. Chem. B* **2007**, *111*, 12508.

[23] S. Bedoui, M. Lopes, S. Zheng, S. Bonnet, G. Molnár, A. Bousseksou, *Adv. Mater.* **2012**, *24*, 2475.

[24] F. Varret, A. Slimani, K. Boukheddaden, C. Chong, H. Mishra, E. Collet, J. Haasnoot, S. Pillet, *New J. Chem.* **2011**, *35*, 2333.

[25] a) T. M. G. Mohiuddin, A. Lombardo, R. R. Nair, A. Bonetti, G. Savini, R. Jalil, N. Bonini, D. M. Basko, C. Galiotis, N. Marzari, *Phys. Rev. B* **2009**, *79*, 205433; b) Z. H. Ni, T. Yu, Y. H. Lu, Y. Y. Wang, Y. P. Feng, Z. X. Shen, *ACS Nano* **2008**, *2*, 2301.

[26] A. H. Castro Neto, F. Guinea, N. M. R. Peres, K. S. Novoselov, A. K. Geim, *Rev. Mod. Phys.* **2009**, *81*, 109.

[27] T. Sato, G. Masuda, K. Takagi, *Electrochim. Acta* **2004**, *49*, 3603.

[28] M. Kepenekian, J. S. Costa, B. Le Guennic, P. Maldivi, S. Bonnet, J. Reedijk, P. Gamez, V. Robert, *Inorg. Chem.* **2010**, *49*, 11057.

**ADVANCED
SCIENCE NEWS**

www.advancedsciencenews.com

**ADVANCED
MATERIALS**

www.advmat.de

[29] C.-H. Park, N. Bonini, T. Sohier, G. Samsonidze, B. Kozinsky, M. Calandra, F. Mauri, N. Marzari, *Nano Lett.* **2014**, *14*, 1113.

[30] S. Das Sarma, S. Adam, E. H. Hwang, E. Rossi, *Rev. Mod. Phys.* **2011**, *83*, 407.

[31] T. Stauber, N. M. R. Peres, F. Guinea, *Phys. Rev. B* **2007**, *76*, 205423.

[32] S. Adam, E. H. Hwang, V. M. Galitski, S. Das Sarma, *Proc. Natl. Acad. Sci. USA* **2007**, *104*, 18392.

[33] a) E. H. Hwang, S. Adam, S. D. Sarma, *Phys. Rev. Lett.* **2007**, *98*, 186806; b) T. Ando, *J. Phys. Soc. Jpn.* **2006**, *75*, 074716.

[34] L. Salmon, G. Molnár, D. Zitouni, C. Quintero, C. Bergaud, J.-C. Micheau, A. Bousseksou, *J. Mater. Chem.* **2010**, *20*, 5499.

1903575 (9 of 9)